

Blipped-Controlled Aliasing in Parallel Imaging for Simultaneous Multislice Echo Planar Imaging With Reduced g -Factor Penalty

Kawin Setsompop,^{1,2*} Borjan A. Gagoski,³ Jonathan R. Polimeni,^{1,2} Thomas Witzel,^{1,4} Van J. Wedeen,^{1,2,4} and Lawrence L. Wald^{1,2,4}

Simultaneous multislice Echo Planar Imaging (EPI) acquisition using parallel imaging can decrease the acquisition time for diffusion imaging and allow full-brain, high-resolution functional MRI (fMRI) acquisitions at a reduced repetition time (TR). However, the unaliasing of simultaneously acquired, closely spaced slices can be difficult, leading to a high g -factor penalty. We introduce a method to create interslice image shifts in the phase encoding direction to increase the distance between aliasing pixels. The shift between the slices is induced using sign- and amplitude-modulated slice-select gradient blips simultaneous with the EPI phase encoding blips. This achieves the desired shifts but avoids an undesired “tilted voxel” blurring artifact associated with previous methods. We validate the method in $3\times$ slice-accelerated spin-echo and gradient-echo EPI at 3 T and 7 T using 32-channel radio frequency (RF) coil brain arrays. The Monte-Carlo simulated average g -factor penalty of the 3-fold slice-accelerated acquisition with interslice shifts is $<1\%$ at 3 T (compared with 32% without slice shift). Combining $3\times$ slice acceleration with $2\times$ inplane acceleration, the g -factor penalty becomes 19% at 3 T and 10% at 7 T (compared with 41% and 23% without slice shift). We demonstrate the potential of the method for accelerating diffusion imaging by comparing the fiber orientation uncertainty, where the 3-fold faster acquisition showed no noticeable degradation. *Magn Reson Med* 67:1210–1224, 2012. © 2011 Wiley Periodicals, Inc.

Key words: parallel imaging; simultaneous multislice; CAIPIRINHA; wideband

Diffusion-weighted imaging and functional MRI (fMRI) are widely used to study the structure and function of the brain. These studies typically rely on rapid, single-

shot two-dimensional (2D) Echo Planar Imaging (EPI) acquisition methods. However, for high-resolution imaging where a large number of slices are needed to cover the brain, a long repetition time (TR) is required. This renders the method inefficient compared with 3D encoding methods (1). Conventional accelerated 2D parallel imaging approaches (2–4) can greatly increase the speed of the EPI encoding by eliminating phase encoding steps. Although beneficial for other reasons, this does not translate to a significant reduction in TR or acquisition time, as diffusion and fMRI sequences contain large, fixed time blocks that cannot be shortened, such as the time for diffusion encoding or the time to a suitable echo time (TE) for T_2^* contrast.

In comparison, accelerating the data acquisition using the simultaneous acquisition of multiple slices can be very effective as it directly reduces the amount of time needed to acquire a fixed number of slices. For example, if three imaging slices are acquired per shot instead of one, the total acquisition time decreases directly by a factor of 3. When $TR > T_1$, e.g., if full-brain coverage is required at high resolution, then the acquisition can maintain a nearly fully relaxed equilibrium magnetization even for $3\times$ acceleration. Furthermore, unlike standard parallel imaging techniques, simultaneous multislice acquisition methods do not shorten the readout period or omit k -space samples. Therefore, they are not subject to a \sqrt{R} penalty on SNR (where R is the acceleration factor) found in conventional parallel imaging acceleration.

Various methods have been proposed for single-shot simultaneous multiplanar imaging including echo volumar imaging and its variants (1,5–8). Multislice methods using slice selection to excite multiple slices simultaneously include the “wideband” imaging (9–11), simultaneous echo refocusing (SER) (12) sometimes referred to as simultaneous image refocused (13) and parallel image reconstruction based multislice imaging (14–17). However, each of these methods has limitations. Echo volumar imaging and its variants offer the advantages of true Fourier-encoded 3D single-shot imaging, but are limited by susceptibility distortions in the slowly encoded k -space direction as well as the difficulty performing the entire 3D trajectory within the T_2^* decay time. Thus, echo volumar imaging requires significant parallel imaging acceleration to begin to overcome these issues (8). The wideband technique applies a slice gradient (G_z) during the readout gradient (G_x) to separate the slices in frequency. While presenting a simple way to disentangle

¹Athinoula A. Martinos Center for Biomedical Imaging, Department of Radiology, Massachusetts General Hospital, Charlestown, Massachusetts, USA.

²Department of Radiology, Harvard Medical School, Boston, Massachusetts, USA.

³Department of Electrical Engineering and Computer Science, MIT, Cambridge, Massachusetts, USA.

⁴Harvard-MIT Health Sciences and Technology, MIT, Cambridge, Massachusetts, USA.

Grant sponsor: 16 National Institutes of Health Institutes and Centers that support the NIH Blueprint for Neuroscience (Human Connectome Project, 1U01MH093765); Grant numbers: K99EB012107, R01EB006847, R01EB007942 (NIH NIBIB grants), P41RR14075 (NCRN grant).

*Correspondence to: Kawin Setsompop, Athinoula A. Martinos Ph.D., Center for Biomedical Imaging, Department of Radiology, Massachusetts General Hospital, Charlestown, MA 02129. E-mail: kawin@nmr.mgh.harvard.edu

Received 1 March 2011; revised 6 June 2011; accepted 20 June 2011.

DOI 10.1002/mrm.23097

Published online 19 August 2011 in Wiley Online Library (wileyonlinelibrary.com).

the slice information, the simultaneous readout and slice gradients cause an undesirable “voxel tilting” effect whereby the readout and slice direction are no longer orthogonal. A simple calculation shows that for standard resolution and field of view (FOV) (e.g., 2 mm isotropic and 20 cm) and with 4 cm slice gaps between simultaneously excited slices, voxel tilting artifact would cause signal from the top of each voxel to shift horizontally ~ 2.5 voxels to one side and the bottom of the voxel to shift ~ 2.5 voxels in the other direction. Thus, the signal from each voxel is smeared over 6 voxels (see Eqs. 6 and 8 in Ref. 16). SER or simultaneous image refocused uses serial excitation of the imaging slices followed by a shared EPI readout. A readout gradient blip between the excitation of the first and second slice time-shifts the location of the gradient echo in the readout for the spins in the first slice. This allows the two slices to be separated by simply separating the first and second half of each readout. But the procedure necessarily lengthens the readout period and thus the total echo train length, increasing susceptibility associated image distortion in EPI.

A second class of simultaneous multislice methods uses parallel imaging concepts to unalias the pixels from slices excited and encoded simultaneously (14). Unfortunately the aliased slices are generally close to each other due to a comparatively smaller FOV in the slice direction. For example, a 60 slice 2-mm isotropic acquisition with $3\times$ multislice acceleration would require unaliasing pixels 4 cm apart in the slice direction. This pixel separation is equivalent to that of a conventional parallel imaging reconstruction for a brain image with a 20-cm FOV_{inplane} and $R = 5$ acceleration. The short distances between aliased pixels place a high demand on the spatial variations in the coil sensitivities and result in unaliasing artifacts and a high g -factor penalty. Parallel imaging based methods have recently been combined with the SER method to extend the number of simultaneous slices (18,19) and this approach has been recently explored for fMRI and diffusion applications (19).

Modifications to the multislice parallel imaging technique have been proposed to mitigate the high g -factor issue. The “controlled aliasing in parallel imaging results in higher acceleration” (CAIPIRINHA) technique (15) introduces an inplane image shift between the simultaneously acquired slices to increase the distance between aliasing voxels and thereby make them easier to separate. For the conventional FLASH acquisitions for which the method was demonstrated, this is achieved by using a different radio frequency (RF) pulse for every other k -space line. The multiband pulse modulates the phase of the magnetization excited in the individual slices for each k -space line. For example, alternating the phase of every other k -space line’s excitation by π will result in a spatial shift of $FOV/2$ in the phase-encoded (PE) direction for that slice. Unfortunately, this technique is not applicable to EPI where all the PE lines are read out after a single RF excitation. An alternative approach, suitable to EPI, was proposed on the basis of the wideband method (10,16). In the first method (10), the wideband technique is not used as the principal method of separating the aliased slices, but is used to assist the parallel imaging method by introducing relative inplane shifts in the readout direction between the simultaneously acquired slices (by applying

a constant slice-select gradient during the readout). In the second method (16), a shift in the PE direction is also applied to introduce further distance between aliasing pixels. The shift in the PE direction is achieved by applying G_z blips simultaneous with the EPI phase encoding blips. In either case, the information from the parallel acquisition is used to dealias the slices and the CAIPIRINHA-style relative image shifts are used to reduce the g -factor. Because the shift is not used to fully separate the slices, it can be smaller than the whole FOV shift that is normally used in the wideband method—which reduces, but does not eliminate, the voxel tilting artifact that results from having the slice gradient and encoding gradient on simultaneously. For example, applying G_z gradient blips simultaneously with the EPI phase encoding blips just translates the tilted voxel problem into the PE direction since now the phase encoding is tilted into the slice direction. With such technique, even with a small shift (e.g., 15% of the FOV), the voxel tilting artifact is non-negligible and the g -factor reduction is limited (16).

In this study, we extend the method of Nunes et al. (16) by introducing a technique termed as “blipped-CAIPI,” which can be used in EPI to achieve spatial shifts in the PE direction between simultaneously excited slices but without the voxel tilt problem. This allows for unrestricted application of image shifts in the PE direction to gain the maximal benefit in g -factor reduction. We show that the method introduces negligible loss of signal or blurring compared with the wideband or blipped-wideband methods. We estimate the resulting g -factor using measured noise-covariance information and a Monte-Carlo pseudo-multiple replicate time-series analysis and demonstrate $3\times$ simultaneous multislice acquisitions in gradient recalled echo (GRE)- and SE-EPI sequences. We also combine the method with $R = 2$ inplane GRAPPA and/or a $2\times$ SER excitation. The combination with the SER method achieved six slices per single-shot (echo train) in a GE-EPI acquisition.

THEORY

A brief explanation of the wideband approach and its associated tilted voxel artifact is provided in the context of achieving an interslice image shift in the EPI PE direction, i.e., blipped-wideband (16). The blipped-CAIPI scheme will then be introduced as a modification to the blipped-wideband approach to remove the tilted voxel artifact. The basic method of imparting a $FOV/2$ shift in the PE direction will be described using an example of a two simultaneously excited slices, one of which is at isocenter, as shown in Fig. 1a. However, a similar analysis applies to cases at off-isocenter locations and to cases with differing numbers of simultaneous slices and interslice image shifts.

The blipped-wideband gradient scheme is shown in Fig. 1b (left). A train of constant gradient blips in the slice-select direction (G_z) is applied simultaneously with the conventional G_y PE blips of the EPI readout (not shown) to create an interslice image shift in the PE direction for the off-isocenter slice (slice 2 at location z_{gap}). The amount of the shift depends on the distance of the slice from isocenter and the area of the blips. For a $FOV/2$ interslice image shift, $\gamma A_{\text{blip}} z_{\text{gap}} = \pi$, where $A_{\text{blip}} = \int_{\text{blip}} G_z dt$ is the area of each blip. Thus, each G_z

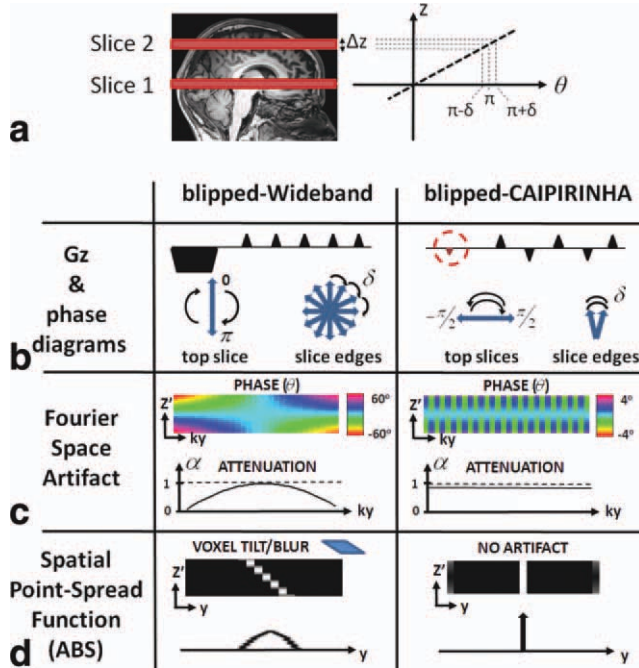


FIG. 1. A description of the blipped-wideband and blipped-CAIPI methods for creating FOV/2 interslice image shift between two simultaneously excited slices (the bottom slice at isocenter) and the source of the blurring artifact (tilted voxel) of the blipped-wideband method. [Color figure can be viewed in the online issue, which is available at wileyonlinelibrary.com.]

blip imparts a π phase increment to the spins located at the center of slice 2, resulting in a FOV/2 image shift relative to slice 1. There is no shift for the isocenter slice.

The voxel tilting artifact associated with this technique arises from the finite thickness, Δz , of the slices. Each G_z blip introduces a $\pm\delta$ phase variation across the slice, where $\delta = \gamma A_{\text{blip}} \frac{\Delta z}{2}$. This causes through-plane intravoxel dephasing and hence signal attenuation by an attenuation factor $\alpha(z', N_y) = \frac{1}{\Delta z} \int_{-d\Delta z/2}^{\Delta z/2} e^{-i\theta(z', k_y)} dz'$. Here $\theta(z', N_y)$ is the phase of the signal as a function of the offset, z' , from slice center, and as a function of the integer index, N_y , indexing the k_y phase encode line. With a train of G_z blips, the phase variation accumulates with each blip. The prewind blip, shown in Fig. 1b (with area A_{prewind}), starts the EPI readout with linear phase relationship across the slice given by $\theta_{\text{prewind}} = \gamma A_{\text{prewind}} z'$ with the value of A_{prewind} chosen to ensure minimum through-plane dephasing for the $k_y = 0$ lines ($A_{\text{prewind}} = -\gamma A_{\text{blip}} N_{\text{TOT}}/2$, where N_{TOT} is the total number of k_y lines). After n blips, $\theta(z', n) = \theta_{\text{prewind}} - \gamma n A_{\text{blip}} z'$.

A diagram of the undesirable additional phase at the edges of each slice is shown in Fig. 1b. Figure 1c shows the phase variation $\theta(z', N_y)$ within the slices as a function of k_y line. At the beginning of the readout, the slope of this phase is negative due to the large negative prewinding G_z lobe. It then increases monotonically due to the G_z blips, exhibiting a zero value at the center k_y line. The corresponding signal attenuation plot is shown in the same panel, with zero attenuation at k -space center and large attenuation at the edge of k -space. Finally, the spatial point-spread function resulting from this k -space

filter is plotted in Fig. 1d. The top plot was obtained by applying an inverse Fourier transform (along k_y) to an magnetic resonance (MR) signal with the phase profile as shown in Fig. 1c. This plot illustrates the undesirable voxel tilting artifact (where the point-spread function at different z' locations is shifted by a different amount). The bottom plot shows the overall spatial point-spread function created by integrating the signal along the slice direction (the same plot can be obtained by taking the inverse Fourier transform of the attenuation plot in Fig. 1c). Here, we assume a homogeneous signal through the slice. The blurring artifact can be very significant. For example, for acquisition with $\text{FOV}_{\text{inplane}} = 20$ cm, slice thickness = 2 mm, and slice gap of 4 cm, a FOV/2 shift via the blipped-wideband approach would cause signal from one voxel to smear over ~ 3.5 voxels.

The blipped-CAIPI technique aims to achieve the same interslice image shift as the blipped-wideband technique but without the undesirable blurring/tilting artifact. This is achieved by modifying the G_z blips so that they impart the desired phase modulation along k_y without causing significant phase accrual over the EPI readout. The diagrams on the right part of Fig. 1b–d illustrate this phase-cycling method. Figure 1b shows the phase-cycled G_z blips which now exhibit a sign reversal on every other PE line. Furthermore, the prewinding lobe has also been replaced by a smaller balancing blip (shown in red), of area $A_{\text{prewind}} = -A_{\text{blip}}/2$. As shown on the same panel, the corresponding phase evolution at the center of the top slice still exhibits the desired π phase increment. However, because of the sign modulation of the G_z blips, the incremental phases at the slice edges no longer accrue over the readout. Rather, they switch back and forth between two small amplitude states—with the A_{prewind} chosen to balance these states so they are center on zero. Figure 1c shows the phase variation within the excited slices which now switches back and forth between two opposing states, $\pm\delta/2$, with the same magnitude of variation. Thus, $\theta(z', N_y) = (-1)^{N_y+1} \gamma A_{\text{blip}} z'/2$. Therefore, the amount of signal attenuation is the same for all k_y lines—resulting in a flat attenuation plot as shown and no filtering effect, and thus a preserved spatial point-spread function. Figure 1d shows the resulting spatial point-spread function which is an ideal delta function for all z positions within the slice but with some FOV/2 ghosting resulting from the phase differences between even and odd lines. The ghost within each slice varies linearly as a function of z (i.e., it is symmetric and of opposing sign at $\pm z$). Assuming no variation in the underlying signal within the slice, the ghosting will cancel for the summed signal along the slice direction. In reality, some minor through-slice signal variation is always present. However, for practical levels of through-plane signal variation, this does not appear to result in significant ghost artifact. For example, consider a rather extreme case where the MR signal has a 90° linear phase variation through the slice. The resulting ghost artifact from the FOV/2 interslice shift is only 1% for an acquisition with $\text{FOV}_{\text{inplane}} = 20$ cm, slice thickness = 2 mm, and a 4-cm spacing between simultaneously excited slices.

The scheme presented in Fig. 1 illustrates the blipped-CAIPI technique for a special case where one of the

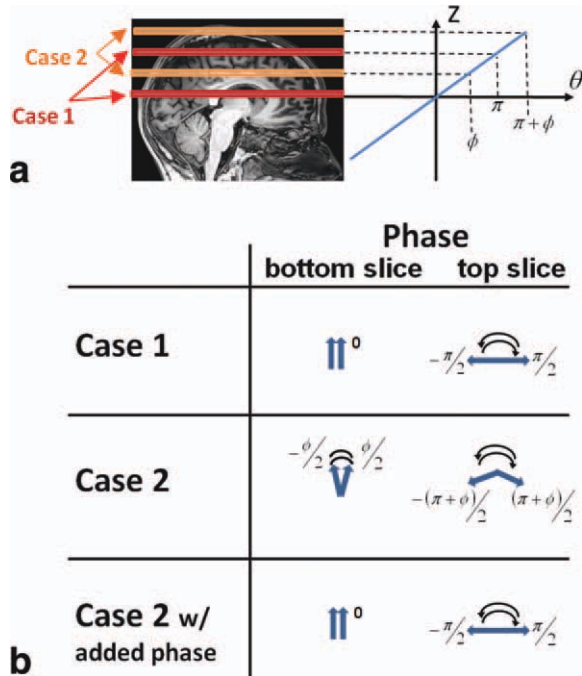


FIG. 2. Generalization of the blipped-CAIPI 2-slice FOV/2 shift method to the case where neither slice is at isocenter. **a:** Case 1, where one slice at isocenter (red), and case 2, the general case with neither slice at isocenter (orange). **b:** The phase at the slice center for the two cases. The resultant slice phases for case 2 are not as desired, which leads to an $N/2$ PE ghost even for the infinitely thin slice condition. This problem can be resolved by adding $+\phi/2$ phase to even k_y lines and $-\phi/2$ phase to odd k_y lines before reconstruction. [Color figure can be viewed in the online issue, which is available at wileyonlinelibrary.com.]

excited slices is at the isocenter position. Figure 2 also shows the case where neither slice is at isocenter (case 2; orange slices in Fig. 2a) as well as the case described above where one of the slices is at isocenter (case 1; red slices). Again, the phase vectors in Fig. 2b represent the signal phase of even and odd k -space lines for each slice. Here, only the slice center is considered (as the through-slice phase variation is unchanged from before). For the nonisocenter case, an application of a single positive G_z blip adds $\pi + \phi$ and ϕ phase at the slice center for the top and bottom slice, respectively, with $\phi = \gamma A_{\text{blip}} z_{\text{offset}}$, where z_{offset} is the offset of the bottom slice from isocenter and again, $\gamma A_{\text{blip}} z_{\text{gap}} = \pi$. The prewind blip is half the area of the G_z blip and acts to symmetrize the phase of the even and odd k_y lines around zero by adding $-\phi/2$ to the bottom slice and $-(\pi + \phi)/2$ to the top slice. The phase at slice center of the even and odd k_y lines are as shown in Fig. 2b. As can be seen, the even and odd k_y lines no longer have the same phase for the bottom slice or an exact π phase difference for the top slice. This leads to an $N/2$ PE ghost even for the infinitely thin slice condition. We address this by adding $+\phi/2$ phase to even k_y lines and $-\phi/2$ phase to odd k_y lines before reconstruction. The key observation is that the phase error is the same in both the bottom and top slices, allowing it to be corrected with a simple phase shift to even and odd k -space lines. With this observation, we

see that the analysis generalizes to cases where more slices are simultaneously excited and to the case where FOV/3 or FOV/4 shifts are desired, in which case the k_y line dependent correction cycles in periods of three or four lines rather than in a period of two lines.

Figure 3 shows the blip schemes and phase diagrams depicting the relative phase between the excited slices for spins at the slice center for various types of interslice shifts (FOV/3, FOV/4 in addition to the FOV/2 shift). The FOV/2 diagram shows the blip pattern and resulting phase of the even and odd lines, which produces a FOV/2 shift for every other slice. This pattern is clearly useful for two simultaneously excited slices, but can also be used for three simultaneously excited slices. In this case, the shifts would be 0, FOV/2 and 0 for the three slices. Thus, a z variation in coil sensitivity patterns is needed to unalias the first and third slices. For a coil without a z variation in coil sensitivity patterns (elements distributed in x and y only), it is desirable to give each slice a unique shift relative to the bottom slice. For example, if three slices are simultaneously excited, then the shifts might be 0, FOV/3, and 2FOV/3. The aliased pixels are then always separated in y . This scheme is shown in the FOV/3 diagram shown in Fig. 3. Similarly, the FOV/4 shifts are useful when four slices are excited and no z variation is present in the coil array, or if five slices are simultaneously excited and the array has some z variation.

Figure 3 also shows the extra phase accrued at the edges of the slices. Because of periodic rewinding of the gradient moment in blipped-CAIPI, no significant phase accrual is allowed to build up over the EPI readout.

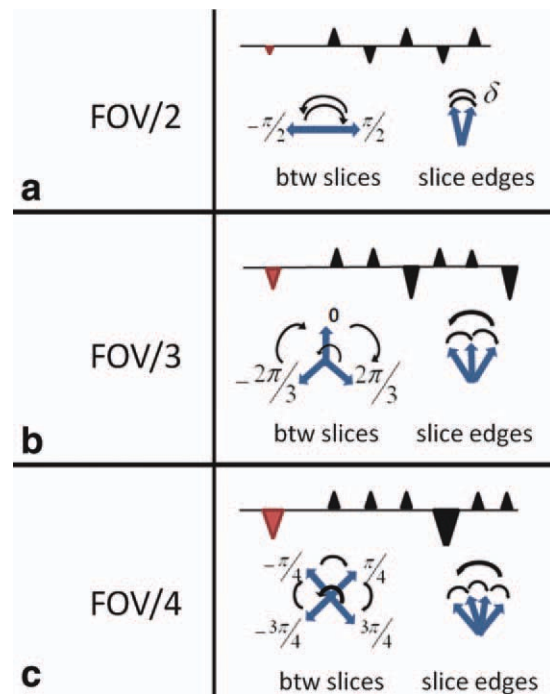


FIG. 3. Generalization of the blipped-CAIPI method to FOV/3 and FOV/4 shifts between successive slices. Each panel shows: top, G_z gradient scheme; bottom, corresponding phase diagrams between excited slices and at slice edges of blipped-CAIPI acquisition for various interslice image shifts. [Color figure can be viewed in the online issue, which is available at wileyonlinelibrary.com.]

Furthermore with the balancing blip in place, the phase states are always centered on the zero phase position. For the FOV/2 shift this was shown to result in complete cancellation of the image ghost when the signal is uniformly distributed through the slice. For other shift factors, the balancing blip reduces the ghost artifact but does not eliminate it. Nonetheless, the ghost level is negligible for typical acquisitions.

As the phase per millimeter imparted by the blip scheme depends on the distance between simultaneously excited slices (e.g. two simultaneously excited slices must receive a π relative phase shift for a FOV/2 shift), the phase incurred across the slice is dependent on the ratio of the slice thickness to the distance between simultaneously excited slices. To assess this effect, we analyze a nearly worst-case example. We assess the ghost level for the somewhat extreme case where a FOV/3 shift is applied to an acquisition with a slice thickness of 2 mm and a 6-mm spacing between simultaneously excited slices. A small distance between simultaneously excited slices is potentially useful for cardiac imaging where FOV_z is small. This resulted in a delta point-spread function with ghosting artifacts at $\sim \pm \text{FOV}/6$ locations. When the balancing blip was used in the acquisition, the resulting ghost level was modeled to be 0.6% and the delta response signal level was found to be 98.5% of the expected (ideal) value when no through-slice signal variation was present. By contrast, the ghost level without the balancing blip was 2.2% and the delta response was 96.4%. We also modeled the case with through-slice signal variation assuming that the signal has a 45° linear phase variation over the slice thickness. Using the balancing blip, the ghost and signal levels were 2.3% and 96% in this case. Without the balancing blip they were 4.2% and 89%.

MATERIALS AND METHODS

Acquisitions

Blipped-CAIPI was implemented in both SE-EPI and GRE-EPI sequences to assess the technique for both diffusion-weighted imaging and fMRI. All acquisitions were obtained from healthy subjects after obtaining informed consent using an institutionally approved protocol. Imaging was performed using Siemens scanners (Siemens Healthcare, Erlangen, Germany) equipped with 32-channel head array coils. The 3T acquisitions used a Siemens whole-body TIM Trio scanner and the commercial 32-channel head array coil and the 7T acquisitions used a 7T Siemens whole-body system equipped with AC84 head gradients (80 mT/m maximum gradient strength and 400 T/m/s maximum slew rate). A custom-built 32-channel RF head array was used for reception, and a custom-built detunable band-pass birdcage coil for transmit (20).

The SE-EPI diffusion-weighted imaging was performed with a twice-refocused sequence (21,22) using either conventional single-slice imaging or a 3× slice-accelerated simultaneous multislice acquisition. No inplane acceleration was used. Imaging parameters were resolution = 2 mm isotropic; FOV = 208 × 208 × 120 mm; partial Fourier = 6/8; bandwidth = 1658 Hz, $b = 1000$ s/

mm², 64 directions, one $b = 0$ image, 60 × 2 mm slices, and TE = 96 ms. For the conventional acquisition, TR = 9 s and the total acquisition time (T_{acq}) was 9.75 min. For the simultaneous multislice acquisition, three slices separated by 4 cm were simultaneously excited with an FOV/2 shift applied to the middle slice (i.e., the scheme depicted in Fig. 3a). The 3× slice-accelerated sequence resulted in TR = 3 s and $T_{\text{acq}} = 3.25$ min.

A GRE-EPI sequence with 1 mm isotropic spatial resolution was acquired at 7 T to illustrate the potential benefit of blipped-CAIPI technique for high-resolution fMRI. The 3× slice-accelerated simultaneous multislice acquisition allowed the whole-brain acquisition (120 slices) with a TR of 2.88 s. For this acquisition, 2× inplane acceleration was used to reduce EPI image distortion. Imaging parameters were resolution = 1 mm isotropic, FOV = 200 × 200 × 120 mm, partial Fourier = 6/8, TR/TE = 2.88 s/24 ms, effective echo spacing = 0.32 ms, bandwidth = 1786 Hz, 120 1 mm slices, and flip angle = 80° (approximately the Ernst angle). The simultaneous multislice acquisition used three simultaneously excited slices separated by 4 cm. Because of the 2× inplane acceleration, an intraslice image shift of FOV/4 was used to prevent voxels with same inplane (x, y) locations of adjacent image slices from overlapping. This was achieved by applying the FOV/2 blipped-CAIPI G_z train to the reduced FOV acquisition.

In addition to these acquisitions, the blipped-CAIPI method was also demonstrated in combination with SER technique to achieve six slices per shot in a 3-T GRE-EPI acquisition. This acquisition used $R = 3$ blipped-CAIPI together with SER to achieve an extra 2× slice acceleration factor. An $R = 2$ inplane acceleration was used to counteract the lengthened echo-spacing produced by the SER method. The SER method increased the echo spacing by ~50%, yielding a net ~25% improvement in susceptibility induced distortion given the $R = 2$ inplane acceleration. The parameters for the acquisition were resolution = 2 mm isotropic, FOV = 208 × 208 × 120 mm, partial Fourier = 6/8, bandwidth = 1093 Hz, TR/TE = 0.77 s/33 ms, effective echo-spacing = 0.525 ms, 60 2 mm slices, and flip angle = 50° (approximately the Ernst angle). A FOV/4 intraslice image shift was used because of the inplane acceleration.

To perform simultaneous multislice excitation, conventional slice-selective RF pulses were frequency modulated and summed. The variable-rate selective excitation (VERSE) method (11) was used to reduce the peak RF voltage and thus the SAR of the excitation pulses. Bloch simulation was used to assess the slice selection performance of the multislice RF pulses in comparison with the standard RF pulses normally used by the system. To compensate for the degradation in the slice selection profile at off-resonance frequencies due to VERSE, the time bandwidth product was increased compared with the conventional pulses. The VERSEed multislice RF pulse was deemed acceptable when (i) the root mean square error of the excited slice profile was approximately equal to or less than that of the standard RF pulse over an off-resonance frequency range of ± 50 Hz, (ii) the sequence would run without exceeding the SAR threshold, and (iii) the pulse duration was below 5.5 ms.

For the SE-EPI acquisitions, the pulses were designed using the Shinnar-Le Roux (SLR) algorithm (10). The VERSE method was applied more heavily to the 180° pulses. For the 90° excitation, the time bandwidth product, VERSE factor, and pulse-length were 6, 3×, and 4.8 ms, respectively. For the 180° refocusing pulses, these parameters were 6, 6×, and 5.38 ms, respectively. The normalized root mean square error from the ideal profile (normalized by the area under the ideal profile) for the 90–180–180° sequence was 17.6% at 0 Hz and 28.5% at ±50 Hz off-resonance for our designed RF pulses. This was an improvement over the standard RF pulse train (27.4% and 32.1% for spins off resonant by 0 Hz and 50 Hz). For the GRE-EPI acquisitions, modulated Hanning-windowed sinc pulses were used with a time bandwidth product, VERSE factor and pulse-length of 6, 3×, and 4.8 ms for both the 3-T blipped + SER acquisition and the 7-T acquisition. For the GRE-EPI, the normalized root mean square error of the slice profile was 20.7% for on resonant spins and 27% for ±50 Hz off-resonance spins. The normalized root mean square error of the standard pulses was 23% and 26%. For the blipped + SER acquisition, the pulse duration reported here represents the duration of each subpulse in the two SER excitations module.

Reconstruction and SNR Quantification

The SENSE algorithm (3) can be directly adapted for simultaneous multislice imaging acquisition (14,15). On the other hand, direct application of the GRAPPA method is less straightforward and previous applications of GRAPPA to slice-aliased data have used a SENSE/GRAPPA combination method (23). Although the method works well for standard multislice acquisitions, direct application of this method causes significant aliasing artifact in multislice acquisitions with interslice image shifts. To overcome this issue, we developed an alternative k -space based parallel imaging approach for multislice imaging, which we term slice-GRAPPA. In brief, the slice-GRAPPA algorithm fits a GRAPPA-like kernel to each slice of a prescan calibration dataset acquired one slice at a time and then applies these kernels to estimate the k -space data of each individual imaging slice from the collapsed slices. Thus, for the 3-fold slice-accelerated acquisition, three separate sets of GRAPPA kernels were fitted and applied, one for each imaging slice. The issues in applying SENSE/GRAPPA to CAIPIRINHA shifted slices and the slice-GRAPPA algorithm are described in detail in Appendix.

For the acquisitions with both inplane and slice acceleration, the reconstructions were performed in sequential steps: first the slice-GRAPPA was applied to separate the aliased slices, then conventional GRAPPA was used to generate the missing k -space lines for the inplane under-sampled slices. For acquisitions at 3 T, the reconstructed images from the individual coil channels were combined using the root sum-of-square method. For acquisition at 7 T where the coil channels are more prone to coupling, a coil noise-covariance-weighted root sum-of-square method was applied to improve SNR.

As with any parallel imaging method, simultaneous multislice technique brings with it nonuniformity in

noise enhancement which complicates the interpretation of the statistical analysis of fMRI activation and diffusion imaging. The SNR performance of the simultaneous multislice technique was calculated using the pseudo-multiple replica method (24) and compared with the SNR of the unaccelerated acquisition also assessed with the pseudo-multiple replica method. We start by applying the pseudo-multiple replica method to fully sampled data (also with no inplane acceleration). The signal level was taken as the average image signal in a 20 image time-series taken from this fully sampled data (one slice per EPI readout), which was taken to be a “noise-free” estimate of the signal. Noise was added to each of these images by drawing from the noise distribution defined by the measured noise-covariance matrix. The SNR is then assessed by computing the mean value of each pixel in the 1000 image pseudo-time-series of the coil-combined images and dividing by its calculated standard deviation over the pseudo-time-series.

For the slice-accelerated case (but without inplane acceleration), the pseudo-time-series of k -space data was formed by aliasing the slice data with or without spatial shifts before adding the noise. In both cases, the appropriate slice-GRAPPA kernel was fit and applied to the pseudo-time-series. For the slice-accelerated case with inplane acceleration, the signal model was derived from the time average of 20 images acquired with conventional ($R = 2$) inplane acceleration and GRAPPA reconstruction (and no-slice acceleration). This was done to ensure that the object shape in all models contained identical B_0 distortions.

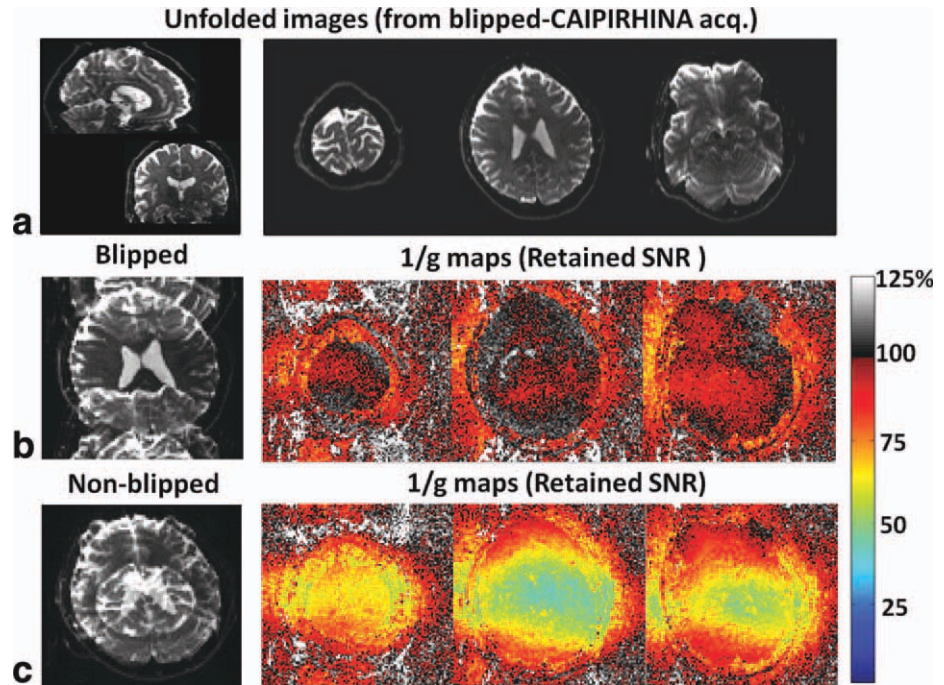
The ratio between SNR maps of the slice-accelerated and conventional acquisitions allowed us to create a map of the “SNR retained” by the image reconstruction. In general, the SNR retained is $1/g\sqrt{R_{\text{inplane}}}$ and for case of no inplane acceleration, the SNR retained is just $1/g$. Thus, for all acquisitions, we plot the $1/g$ maps as determined by the SNR retained calculation. The g -factor calculations were obtained for simultaneous multislice acquisition both with and without interslice image shift to assess the effect of CAIPIRINHA shifts. Values for $1/g_{\text{ave}}$ were obtained from a brainlike region of interest (ROI).

Nonaccelerated and 3× slice-accelerated diffusion-weighted imaging acquisitions were compared using qualitative and quantitative metrics from FSL (25). First, tensor-derived, directionally encoded color maps for both datasets were generated and compared. Furthermore, bedpost (26) was used to estimate samples from the posterior probability density function of the principal and crossing fiber orientations of both acquisitions. These estimated samples of the probability density functions were used to calculate and map the 95% uncertainty angle for the first and second fiber orientations.

RESULTS

Figure 4a shows the results of the 3× slice-accelerated blipped-CAIPIRINHA SE-EPI acquisition, including views of an unaliased 3D stack of slices and the corresponding unaliased slice group. Figure 4b shows the blipped-CAIPI aliased slice and the corresponding g -factor maps. Figure 4c shows the same information for the

FIG. 4. Results from $3\times$ slice-accelerated SE-EPI acquisition with FOV/2 interslice shift. **a:** Unfolded images of the unaliased 3D volume; left: coronal and sagittal views and right: axial views of an unaliased slice group. **b:** Left: aliased image of blipped-CAIPI slices. Right: the corresponding Monte-Carlo generated retained SNR maps of the unfolded slices. **c:** Aliased slice group and $1/g$ maps for $3\times$ slice-accelerated acquisition without interslice shift. With blipped-CAIPI interslice shift, SNR retention is close to 100% in all locations, whereas for the acquisition without the shift the SNR retention drops to as low as 50% in some areas of the image. [Color figure can be viewed in the online issue, which is available at wileyonlinelibrary.com.]



nonblipped acquisition. The $1/g$ average \pm standard deviation in the brain region was 0.997 ± 0.08 for the blipped-CAIPI and 0.68 ± 0.14 for nonblipped simultaneous multislice method indicating an average SNR improvement of 47%. Furthermore, the blipped-CAIPI acquisition reduced the peak g -factor penalty (taken from the peak g -factor after smoothing the g -maps with a 5×5 voxel square kernel) by more than a factor of 2 ($1/g_{\text{peak}}$ of 0.84 vs. 0.41) and thereby provided an SNR improvement of $>100\%$ in the high noise enhancement region. For this acquisition, the blipped-wideband technique (16) would have produced a voxel tilting artifact of ~ 3.5 voxels.

Figure 5 shows the diffusion orientation color-coded fractional anisotropy maps for conventional nonacceler-

ated slices and a blipped-CAIPI $3\times$ slice-accelerated acquisition. Figure 5 also shows maps of the 95% uncertainty angle for the estimation of the principal (fiber 1) and crossing (fiber 2) fiber orientations for the two acquisitions. As expected, the uncertainty of the principal fiber orientation is low in white matter. Furthermore, the uncertainty of the estimates of the secondary crossing fiber (where determined to exist) are low in putative crossing fiber regions such as the anterior region of the corona radiata (indicated by white arrows). These metrics show nearly identical uncertainties for the nonaccelerated and accelerated acquisitions despite the $3\times$ shorter acquisition time of the simultaneous multislice method.

Figure 6 shows a whole-brain 7 T GRE-EPI acquisition at 1 mm isotropic resolution which utilized $3\times$ slice and

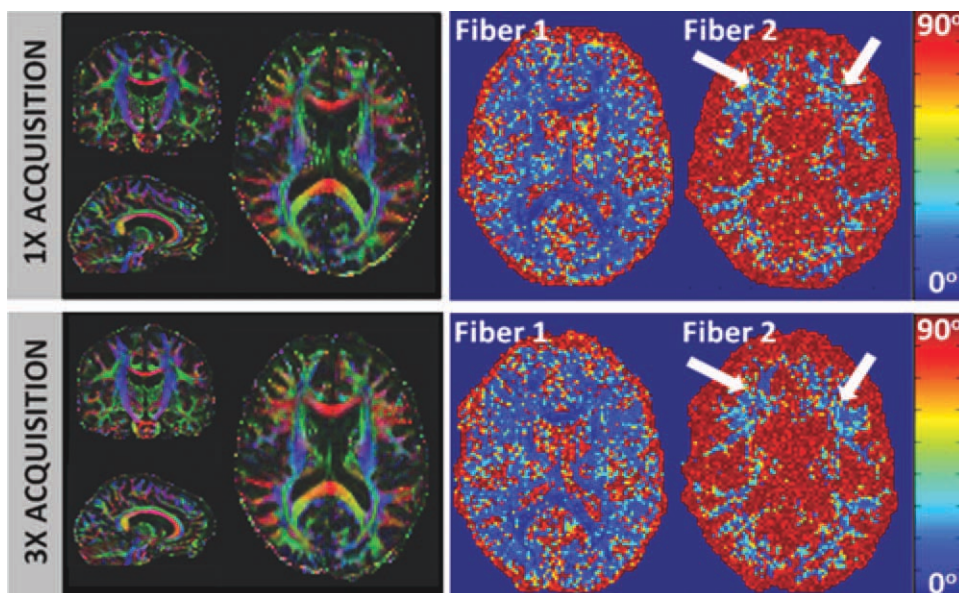


FIG. 5. Diffusion imaging results from a conventional unaccelerated acquisition (top row) and $3\times$ slice-accelerated acquisition with FOV/2 interslice shift (bottom row). Left: directionally encoded diffusion color maps; right: maps of the 95% uncertainty angle for estimate of the principal (fiber 1) and crossing (fiber 2) fiber orientations. [Color figure can be viewed in the online issue, which is available at wileyonlinelibrary.com.]

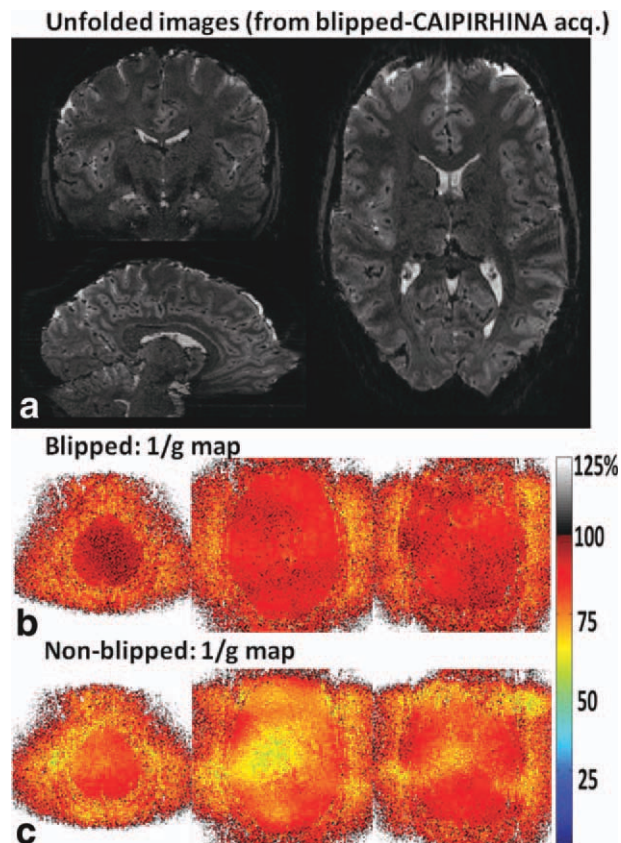


FIG. 6. Example of 1-mm isotropic whole-brain GRE-EPI blipped-CAIPI acquisition at 7 T with $3\times$ slice and $2\times$ inplane acceleration ($TR = 2.88$ s). **a**: Coronal, sagittal, and axial views of the unaliased 3D volume. **b** and **c**: Corresponding $1/g$ map of a representative slice group for blipped-CAIPI and nonblipped acquisition, respectively. [Color figure can be viewed in the online issue, which is available at wileyonlinelibrary.com.]

$2\times$ inplane acceleration. The top panel displays the coronal, sagittal, and transverse views of a single reconstructed volume acquired at a TR of 2.88 s using the blipped-CAIPI method. The bottom panel shows the corresponding $1/g$ -factor map for a representative slice group. The $1/g_{ave}$ in the brain region was 0.90 ± 0.06 for the blipped-CAIPI and 0.77 ± 0.08 for nonblipped simultaneous multislice method indicating an average SNR improvement of 17%. Peak $1/g$ was reduced from 0.57 vs. 0.8 by the blip scheme suggesting an SNR improvement 40% in these high noise enhancement regions.

Figure 7 shows the results of the 2-mm isotropic resolution GRE-EPI acquired with six slices per shot (i.e., $3\times$ slices unaliased with the blipped-CAIPI parallel imaging method and $2\times$ slices separated with the SER method). Thus, two groups of slices are shown marked in red and yellow showing the two SER groups. The coronal and sagittal views of a blipped-CAIPI unaliased slice stack are shown with the slice locations of the six slices sharing the EPI readout. Reduced contrast between gray and white matter is observed as a result of the short TR (0.77 s). The $1/g$ maps of the blipped and nonblipped acquisitions are shown for all six slices. The blipped-CAIPI acquisition results in substantially higher average SNR,

with $1/g_{ave} = 0.81 \pm 0.12$ compared with 0.59 ± 0.12 for the nonblip case showing a 37% slice-average SNR improvement by utilizing the blipped-CAIPIRHINA method. Peak $1/g$ was reduced from 0.33 to 0.57 by the blip scheme suggesting an SNR improvement of 73% in these high noise enhancement regions.

DISCUSSION AND CONCLUSION

In this work, we introduce a blipped-CAIPIRHINA EPI acquisition to shift the image slices of successive simultaneously acquired slices to improve the ability of parallel imaging to unalias the simultaneously excited slices. The method was demonstrated for gradient- and spin-echo EPI acquisitions and assessed using Monte-Carlo estimated g -factor maps as well as visual comparisons and comparisons of the uncertainty of the principal diffusion directions in a diffusion acquisition. The method achieves a 3-fold reduction of TR and thus a 3-fold reduction in the time needed to acquire a whole-brain dataset. For the acquisitions demonstrated (and many applications requiring a large number of slices), the reduction of TR still maintains a $TR > T_1$. If TR was reduced significantly below T_1 (such as the six slice acquisition utilizing $3\times$ simultaneous multislice and $2\times$ SER slice acceleration), reducing the flip angle from 90° to the Ernst angle will improve the SNR of gradient-echo acquisitions. For spin-echo (SE) acquisitions, SNR per unit time is maximized for $TR = 1.25T_1$ and reductions in TR below this are not advantageous from an SNR perspective. For SE-EPI, the conventional high angular resolution diffusion imaging (HARDI) acquisition acquired in 10 min was obtained in just over 3 min with no appreciable artifact or loss in SNR. Thus, the blipped-CAIPI method may facilitate acquisition of HARDI/Q-ball or diffusion spectrum imaging (DSI)-based diffusion imaging in a clinically relevant time frame.

For a GRE-EPI sequence suitable for fMRI acquisition, the method was used to demonstrate whole-brain 1-mm isotropic acquisition at a TR of less than 3 s. Finally, blipped-CAIPI was combined with the SER technique to achieve a rapid six slices per shot acquisition that provides 2-mm isotropic whole-brain coverage in 0.77 s, which improves the ability to perform event-related studies (27) and aids functional imaging experiments desiring rapid temporal sampling of the hemodynamic response (e.g., to better observe its initial transient onset) and/or experiments requiring a fully Nyquist-sampled respiratory cycle.

Recently, Feinberg et al. (19) applied a combination of the SER method with parallel imaging based methods to separate the simultaneously acquired slices for a 6-fold higher sampling rate in resting-state functional brain networks study, and demonstrated a notable 60% increase in peak functional sensitivity. However, the multiplexed EPI method of Feinberg et al. (19) does not attempt to mitigate the high g -factor penalties incurred with high acceleration factors. The proposed blipped-CAIPI method explicitly addresses this noise enhancement by shifting the superimposed slices with a phase ramp, thus reducing the g -factor penalty. This benefit should be especially pronounced for applications such as diffusion imaging where thermal noise dominates.

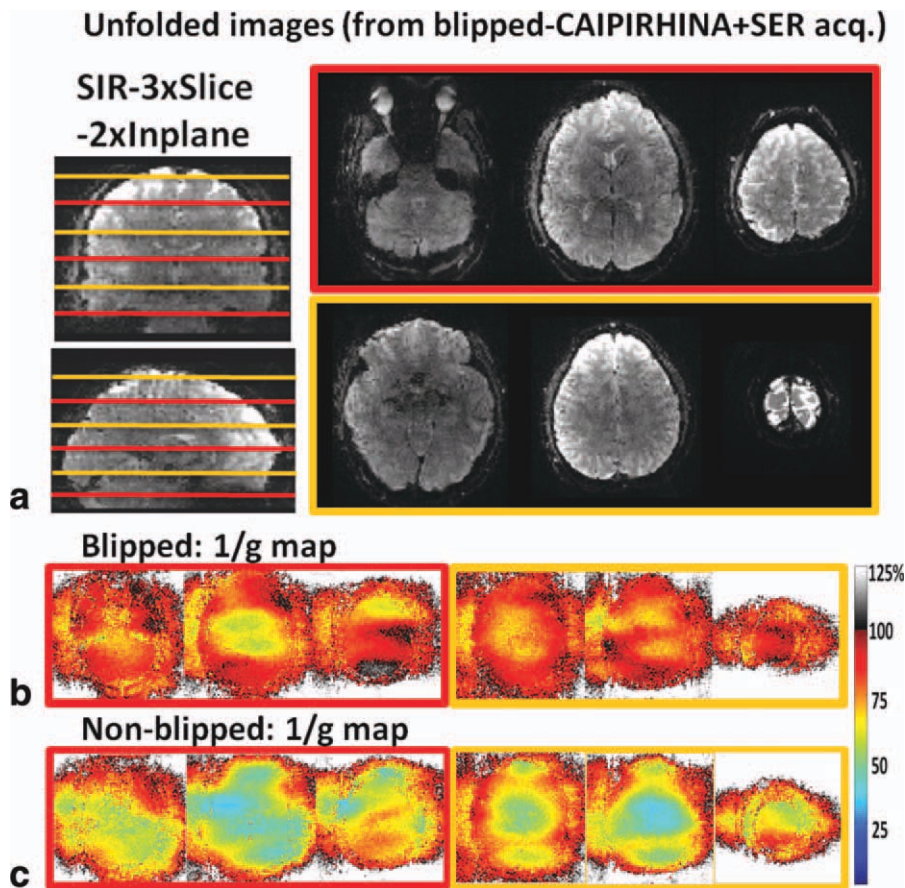


FIG. 7. The six-slice per shot GRE-EPI at 3 T acquired using the SER method ($2\times$) and $3\times$ slice blipped-CAIPI acceleration with $2\times$ inplane GRAPPA. **a**: Left: coronal and sagittal views of the unfolded slice volume with the 2 SER excited slice groups shown in red and yellow. Right: the corresponding six unaliased slices that were acquired with the single EPI readout. **b** and **c**: The $1/g$ maps of the six-slice group acquire with the blipped-CAIPI and nonblipped acquisition, respectively. Peak $1/g$ was reduced from 0.33 to 0.57 by the blip scheme resulting in a SNR improvement of 73%. [Color figure can be viewed in the online issue, which is available at wileyonlinelibrary.com.]

To obtain an absolute SNR comparison between accelerated blipped-CAIPI and nonaccelerated acquisitions, differences in TR and hence T_1 recovery period need to be accounted for. The $3\times$ accelerated SE-EPI acquisition used in this work has a TR of 3 s, while the nonaccelerated acquisition has a TR of 9 s. White matter (T_1 of ~ 850 ms at 3 T (28)) is the main focus of diffusion imaging. Therefore, the signal loss due to saturation effects in the accelerated acquisition is $\sim 3\%$. With low g -factor penalty, the SNR of the slice-accelerated acquisition is very similar to the nonaccelerated case (despite the $3\times$ shorter acquisition time). This was confirmed by the nearly identical directionally diffusion metrics of the accelerated and nonaccelerated acquisitions in Fig. 5. For acquisitions with even shorter TR, the saturation effect lowers the SNR in a given acquisition, but the SNR per unit time is still improved until $TR < 1.25T_1$. For GRE-EPI acquired at the Ernst angle, the SNR per unit time (signal strength divided by \sqrt{TR}) increases as TR is reduced (29,30), until the g -factor penalty overcomes the increasingly marginal SNR per unit time gains as TR is brought below T_1 . We also note that as TR decreases ($TR < T_1$), an interleaved slice excitation pattern become less effective at reducing saturation effects in the overlap region of the imperfect slices. This will result in undesirable signal loss that can be partly mitigated by using RF pulses with sharper slice excitation profiles. This is less of a problem for applications such as high-resolution fMRI and Q-ball diffusion where the number of slices needed is high (60–120). In this case,

even with $R = 3$ simultaneous multislice, the TR will still be relatively high (> 2 s) and the interleaves will be separated by more than T_1 .

The blipped-CAIPI technique can be thought of as a way to modify the aliasing pattern of simultaneous multislice EPI acquisition to better suit the geometry of typical receive array coils. For the 32-channel coil array used in this work, the coil elements are approximately uniformly distributed around the head (with some reduction in ability to unalias pixels aliased in the z -direction). In such a configuration, the parallel imaging performance is similar in all spatial directions. For a $2\times$ slice-accelerated case, it is clear that the best shift is $FOV/2$. Also, if one only considers unaliasing between adjacent slices in the $3\times$ slice-accelerated case, the same holds. But, considering all three slices, there may be a tradeoff where a smaller shift between slices, but one extending across all slices, allows a better unaliasing of slices 1 and 3. For example, a scheme where slices 1, 2, and 3 in a simultaneously acquired slice group have center shifts of 0, $FOV/3$, and $2FOV/3$ instead of the 0, $FOV/2$, and 0 strategy used might perform better as slices 1 and 3 will have a relative shift. In picking the optimal interslice shift for our acquisitions, we perform g -factor performance analysis for different choices of interslice shift using the pseudo-multiple replica method (24). For our 3 T, 32-channel acquisition with $3\times$ slice acceleration, we tested the g -factor performance of both $FOV/2$ and $FOV/3$ interslice shift and found the performance of the $FOV/2$ shift to be marginally better ($1/g_{ave}$ of 0.997 vs. 0.96). It seems

that for the FOV/3 shift case, the benefit of the increased distance between the most distant slices is outweighed by the degradation to the center slice which is now shifted less compared with its neighbors. We note that the FOV/3 interslice image shift will cause a 2FOV/3 image shift differences between the top and bottom slice. However, because of the wrap around effect, the actual distance between the aliased pixel pairs from these two slices will be 2FOV/3 for only 1/3 of all the voxels and FOV/3 for the rest. Similar results were also obtained for the 7-T acquisition with $3\times$ slice and $2\times$ inplane. Here, the FOV/4 interslice shift marginally outperformed the FOV/6 shift ($1/g_{\text{ave}}$ of 0.9 vs. 0.87).

For a coil array with elements distributed along the x - y plane with no z -variation, the aliased voxels need unique x - y locations to be separable. In such case, the largest feasible choice of interslice image shift for axial slices is FOV/3 for a $3\times$ simultaneous multislice acquisition. This will be the optimal choice. For sagittal and coronal acquisitions using an array with no z -axis distribution, the inplane image shift is not helpful when the PE direction is along z . For other coil geometries, the g -factor performance of the blipped-CAIPI acquisition with a given interslice image shift depends on the coil geometry and the distance between aliasing pixels in a nontrivial manner. Nonetheless, the pseudo-multiple replica method can be used to determine the ideal choice of interslice image shift in a case by case basis.

In the blipped-CAIPI method, inplane acceleration places a constraint on the image shift. This constraint is required to prevent the inplane shift from overshifting the already aliased inplane pixels so that they superimpose in the collapsed slices. For this reason, we used a FOV/4 shift for $R_{\text{inplane}} = 2$. This limits the maximal distances between the aliasing voxels and reduces the g -factor mitigation benefit of blipped-CAIPI. In this respect, slice acceleration and inplane acceleration begin to compete with one another. Nonetheless, good SNR performance can still be achieved—as evident in the g -factor maps of the 3-T and 7-T GRE-EPI acquisitions with $3\times$ slice-GRAPPA and $2\times$ inplane acceleration (see Figs. 6 and 7). We note that for $R_{\text{inplane}} = 2, 3,$ and 4 , a FOV/4, FOV/6, and FOV/8 shifts are needed, respectively. However, the blip scheme needed for these shifts is the same as that used for a FOV/2 shift for the $R_{\text{inplane}} = 1$ case. For example, Fig. 6 shows the $R_{\text{inplane}} = 2$ image with a FOV/4 shift implemented with the same blip scheme as the $R_{\text{inplane}} = 1$ FOV/2 shift case.

The average g -factor ($1/g_{\text{ave}} = 77\%$; $g_{\text{ave}} = 1.3$) of our nonblipped 7-T $R_{\text{slice}} \times R_{\text{inplane}} = 3 \times 2$ axial plane acquisition agrees well with that of Moeller et al. (17). They report an average g -factor of ~ 1.5 in a nonblipped coronal plane acquisition with $R_{\text{slice}} \times R_{\text{inplane}} = 4 \times 4$ but with a coil configuration with more elements aiding the acceleration (circumferentially distributed) and a FOV in the phase encode and slice direction chosen so the degree of aliasing was similar to what our axial acquisition would experience for a 3×3 acceleration.

Simultaneous multislice acquisitions require the use of simultaneous multislice RF-modulated excitation pulses, which can lead to high SAR levels. In this work, the

VERSE algorithm was used to alleviate this issue, at a cost of degraded slice selection profile at off-resonance frequencies (which was in turn mitigated by increasing the time bandwidth product). To limit slice degradation, minimal amount of VERSEing should be used to allow the sequence to stay within the SAR limits. It is important to note that the SAR limits as well as the voltage requirement (for a given flip angle) are both patient specific. Therefore, a sequence with a given RF pulse would be under the SAR limits for one subject and might not be for another. For example, the $R_{\text{multislice}} = 3$ accelerated GRE-EPI acquisition at 7 T used in this work required a VERSE factor of 3 to ensure sufficient SAR margin such that this acquisition could routinely run in extended runs for all subjects. By contrast, a VERSE factor of 2 appears to be borderline, i.e. it triggers the SAR monitor for about half the subjects tried.

Parallel imaging based simultaneous multislice acquisition provides an efficient way to dramatically accelerate EPI acquisitions. The proposed blipped-CAIPI technique explicitly reduces the noise amplification incurred by such methods, allowing dramatic scan time reduction with very minor noise penalty. For diffusion imaging, this enables data acquisition with an increased number of diffusion directions and/or higher spatial resolution. In clinical settings, the scan time reduction could facilitate a wider adoption of HARDI/Q-ball or DSI-based diffusion imaging—techniques which provide more robust and detailed information about the local diffusion environment but require acquisitions that are typically too long for many clinical applications. For fMRI acquisitions, the reduction in scan time translates to an increase temporal sampling and/or an increase in spatial coverage. This is particularly important for high-resolution resting-state fMRI studies, where whole-brain acquisitions are required (19).

APPENDIX: THE SLICE-GRAPPA RECONSTRUCTION

First, we briefly describe the SENSE/GRAPPA approach previously used for unaliasing simultaneous multislice acquisitions (23) to explain the artifact which arises when it is applied to acquisitions with interslice image shifts. We then show that the slice-GRAPPA method works well for multislice acquisitions in general—with or without interslice image shifts. For illustration, the formalism presented describes a two-slice acquisition, but the method is easily generalized to more simultaneous slices.

SENSE/GRAPPA Method

The SENSE/GRAPPA technique relies on a relationship illustrated in Fig. A1a. The left of the figure shows a concatenation of two imaging slices as they would appear if acquired by conventional single-slice excitation. Following Fig. A1a from left to right, the k -space data of the concatenated slices are undersampled by $2\times$ and reconstructed with the inverse discrete Fourier transform to produce the aliased multislice image. The SENSE/GRAPPA approach exploits this relationship in

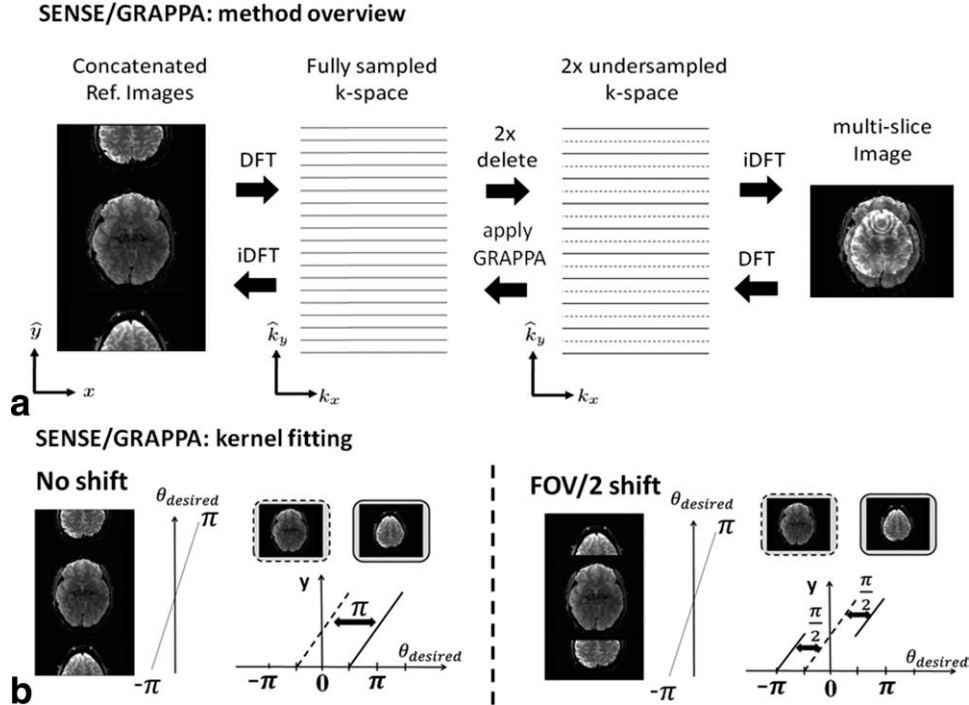


FIG. A1. **a:** The underlying relationship in the SENSE/GRAPPA algorithm proposed by Blaimer et al. (23), where an undersampling of a concatenated image's k -space data results in a slice-collapsed image and, conversely, application of the GRAPPA operator to the aliased data generates a concatenated but unaliased version of the two slices. **b:** Phase variations in the PE direction (y) that have to be synthesized in order for the governing equation of the SENSE/GRAPPA algorithm to be satisfied for the nonshift (left) and shifted (right) $2\times$ multislice acquisitions. Shown are the desired phase variations in the concatenated image space and in the standard image space for each of the simultaneously acquired slices. For FOV/2 shift acquisition, a discontinuity in phase exists in the desired phase variation profile for one of the slices. This condition is difficult to satisfy with smooth coil sensitivities and small GRAPPA kernels, resulting in an unaliasing artifact.

the reverse direction. Viewing Fig. A1a from right to left, the k -space data of the acquired aliased multislice image are viewed as a $2\times$ undersampled dataset. A GRAPPA kernel trained on concatenated reference images (acquired one slice at a time) is applied to the undersampled k -space data to generate the full k -space which can be converted to an unaliased, but concatenated, image of the slices by applying the discrete Fourier transform operator.

The equation for the fitting or application of the SENSE/GRAPPA kernel is given by

$$\begin{aligned} & \hat{S}_j(k_x, \hat{k}_y - m\Delta\hat{k}_y) \\ &= \sum_{\ell=1}^L \sum_{b_x=-B_x}^{B_x} \sum_{b_y=-B_y}^{B_y} n_{j,m,\ell}^{b_x,b_y} \hat{S}_\ell(k_x - b_x\Delta k_x, \hat{k}_y - b_y N_{\text{slice}}\Delta\hat{k}_y) \end{aligned} \quad [\text{A1}]$$

where \hat{y} and \hat{k}_y are the image and k -space coordinates of the PE direction of the concatenated image, $\hat{S}_j(k_x, \hat{k}_y - m\Delta\hat{k}_y)$ is the estimate of the missing k -space data of the j th coil at location $m\Delta\hat{k}_y$ away, $n_{j,m,\ell}^{b_x,b_y}$ is the GRAPPA weight coefficient at location (b_x, b_y) in the GRAPPA kernel for the ℓ th coil used to help synthesize the missing data of the j th coil at a k -space location $m\Delta\hat{k}_y$ away, and N_{slice} is the number of simultaneously excited slices. Thus in image space

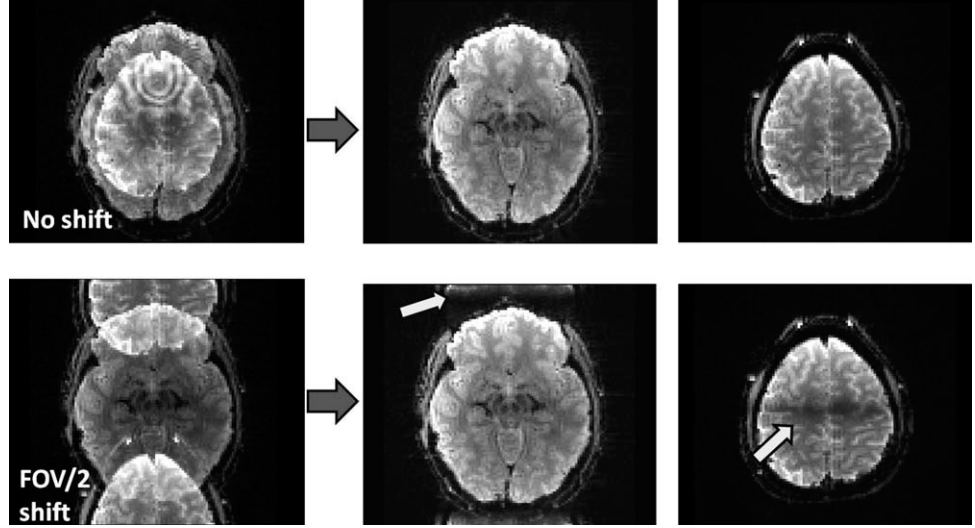
$$\begin{aligned} & \int_x \int_{\hat{y}} \hat{C}_j(x, \hat{y}) \hat{\rho}(x, \hat{y}) e^{-i2\pi(k_x x + (\hat{k}_y - m\Delta\hat{k}_y)\hat{y})} dx d\hat{y} \\ &= \sum_{\ell=1}^L \sum_{b_x=-B_x}^{B_x} \sum_{b_y=-B_y}^{B_y} n_{j,m,\ell}^{b_x,b_y} \\ & \times \int_x \int_{\hat{y}} \hat{C}_\ell(x, \hat{y}) \hat{\rho}(x, \hat{y}) e^{-i2\pi((k_x - b_x\Delta k_x)x + (\hat{k}_y - b_y N_{\text{slice}}\Delta\hat{k}_y)\hat{y})} dx d\hat{y} \end{aligned} \quad [\text{A2}]$$

where $\hat{C}_j(x, \hat{y})$ is the coil sensitivity profile of the j th coil and $\hat{\rho}(x, \hat{y})$ is the underlying image in concatenated image space.

Utilizing the orthogonality property of the Fourier transform to remove the integrals and canceling out common terms results in the following governing equation:

$$\begin{aligned} & \hat{C}_j(x, \hat{y}) e^{-im\Delta\hat{k}_y\hat{y}} = \sum_{\ell=1}^L \hat{C}_\ell(x, \hat{y}) \\ & \times \left[\sum_{b_x=-B_x}^{B_x} \sum_{b_y=-B_y}^{B_y} n_{j,m,\ell}^{b_x,b_y} e^{i2\pi(b_x\Delta k_x x + b_y N_{\text{slice}}\Delta\hat{k}_y\hat{y})} \right] \\ &= \sum_{\ell=1}^L \hat{C}_\ell(x, \hat{y}) \hat{K}_{j,m,\ell}(x, \hat{y}) \end{aligned} \quad [\text{A3}]$$

FIG. A2. Unaliasing artifact produced by applying the SENSE/GRAPPA method to slice-shifted data (bottom) compared with data acquired without the slice shift (top). For the shifted acquisition, residual aliasing artifact can be observed corresponding to locations of discontinuity in the desired phase variation (white arrows).



where $\hat{K}_{j,m,\ell}(x, \hat{y})$ represents the image-domain representation of the GRAPPA kernel (31). In particular, $\hat{K}_{j,m,\ell}(x, \hat{y})$ contains only relatively low-frequency modulations in the concatenated image domain. Note that this modulation repeats every $\text{FOV}/N_{\text{slice}}$ along \hat{y} . As the concatenated image contains both slices, the GRAPPA kernel only has the ability to create common mode modulations along y but cannot impose different phase modulations between the imaging slices.

This governing equation (Eq. A3) is not used for fitting or applying the GRAPPA kernel, but represents the relationship between the coil sensitivity profiles and the GRAPPA kernel. The ability of the SENSE/GRAPPA technique to unalias a particular collapsed image is determined by how well the governing equation can be satisfied for that dataset. Thus, the details of how the phase factor $e^{im\Delta k_y \hat{y}}$ on the left-hand side of the governing equation varies across the concatenated and separated images are critical in determining how well the GRAPPA reconstruction will unalias the slices. Figure A1b illustrates the phase roll of this $\theta_{\text{desired}} = m\Delta k_y \hat{y}$ for the two slice ($m = 1$) acquisition. Both cases are shown—with and without the interslice shift in the y -direction. In the concatenated imaging space, θ_{desired} is a continuous linear function of \hat{y} for both cases (left-hand side plots in Fig. A1b). As a function of y in the separated images, θ_{desired} is shifted by π for the top slice of the no-shift case but is still linear and continuous (Fig. A1b, left). For the FOV/2 simultaneous multislice acquisition (Fig. A1b, left), θ_{desired} is continuous and unshifted for the bottom slice, but discontinuous for the top (FOV/2 shifted) slice. The phase shift between the two slices is $\pi/2$ for this case. As the phase difference between slices must be generated by the coil sensitivity patterns (as previously mentioned, the GRAPPA kernel only provides the common mode variation), the smaller phase difference between slices suggests that the GRAPPA governing equation will be more closely fulfilled for the FOV/2 shift case.

The discontinuity in $\theta_{\text{desired}}(y)$, however, is extremely difficult to produce using the combination of slowly varying coil profiles and the low-frequency modulation

in the image-domain GRAPPA operator. As a result, the SENSE/GRAPPA technique is ill-equipped to satisfy the GRAPPA governing equation for the FOV/2 simultaneous multislice case. This is illustrated in Fig. A2 where the SENSE/GRAPPA algorithm is used to unalias standard, nonshifted multislice (top) and a FOV/2 image-shifted multislice acquisition (bottom). Both were obtained using a 32-channel coil array at 3 T. For standard, non-shifted multislice acquisition, the slice separation is very clean. By contrast, the FOV/2 image-shifted acquisition shows significant artifact in the areas of the phase discontinuity.

Slice-GRAPPA Method

The slice-GRAPPA algorithm is outlined in Fig. A3a. Here, GRAPPA-like kernels are fit using data acquired from separately excited conventional single-slice data. The kernel sets are applied directly to the k -space data of the collapsed images. Two sets of GRAPPA kernels are used to generate each of the two imaging slices. The fitting equation for the algorithm is

$$S_{j,z}(k_x, k_y) = \sum_{\ell=1}^L \sum_{b_x=-B_x}^{B_x} \sum_{b_y=-B_y}^{B_y} n_{j,z,\ell}^{b_x,b_y} S_{\ell,\text{collapse}} \times (k_x - b_x \Delta k_x, k_y - b_y \Delta k_y). \quad [\text{A4}]$$

Thus, each of the two kernel sets $n_{j,z,\ell}^{b_x,b_y}$ (one for each slice) is a set of 32×32 kernels (32 kernels to generate data for each of the 32 coil elements), $S_{j,z}(k_x, k_y)$ is the k -space data of the j th coil at slice location z , $n_{j,z,\ell}^{b_x,b_y}$ is the weight coefficient at location (b_x, b_y) in the GRAPPA kernel of the ℓ th coil that is applied on the collapsed data $S_{\ell,\text{collapse}}(k_x, k_y)$ to help synthesize the missing data of the j th coil at slice location z . Thus, unlike conventional GRAPPA where the kernels operate on the acquired k -space data to fill in missing lines, the slice-GRAPPA kernels create entirely new set of k -space data for each coil of a given slice.

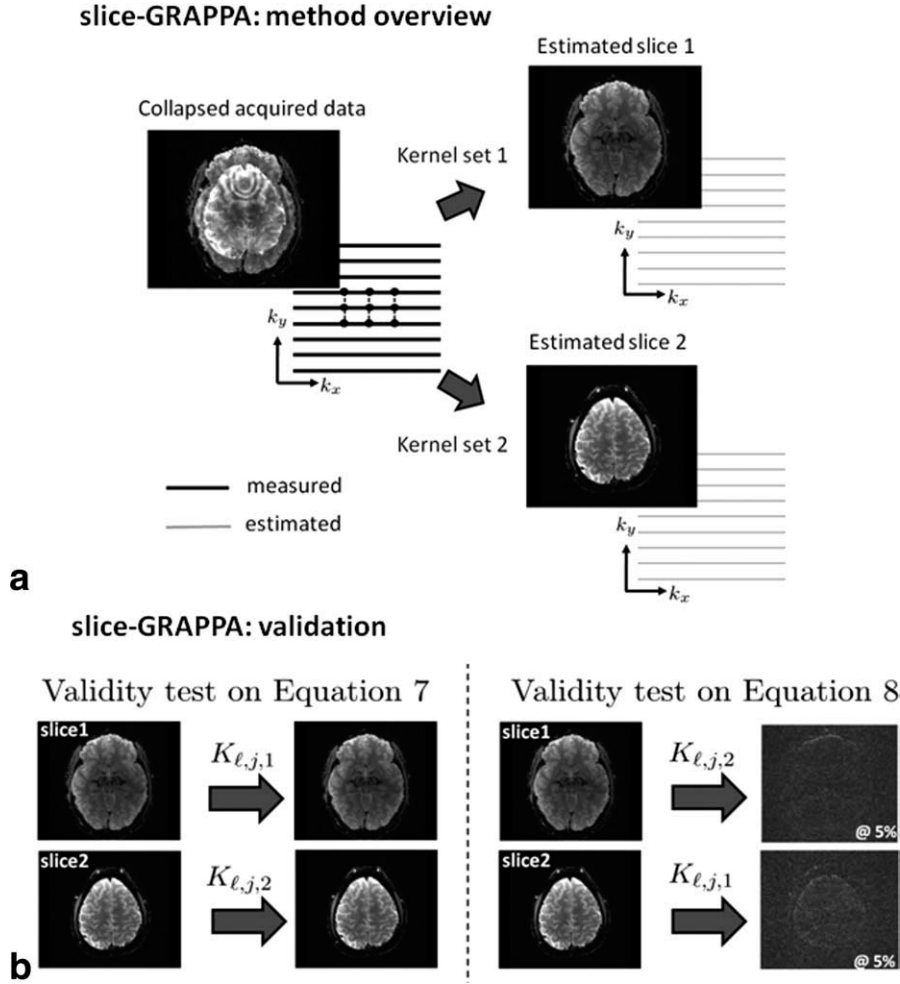


FIG. A3. **a**: Schematic of the slice-GRAPPA algorithm to obtain the k -space data for the unaliased slices. A set of GRAPPA kernels is applied to the k -space data of the aliased slices to generate k -space datasets for each slice. One kernel set is needed for each slice. The kernels are trained from a conventional fully slice-sampled dataset. **b**: Tests of the validity of the simplified governing equations of the slice-GRAPPA algorithm in brain data. This relationship exists between the coil sensitivity profiles and GRAPPA kernel, and should be independent of the underlying anatomy in the image.

Similar to the analysis performed for the SENSE/GRAPPA algorithm, the governing equation for slice-GRAPPA can be obtained by expanding and simplifying the fitting equation (Eq. A4) which results in

$$\begin{aligned}
 C_{j,z}(x,y)\rho_z(x,y) &= \sum_{\ell=1}^L C_{L,\text{collapse}}(x,y)\rho_{\text{collapse}}(x,y)K_{\ell,j,z}(x,y) \\
 &= \sum_{\ell=1}^L \left\{ \sum_{sl=1}^{N_{\text{slice}}} C_{\ell,sl}(x,y)\rho_{sl}(x,y) \right\} K_{\ell,j,z}(x,y) \\
 &= \sum_{sl=1}^{N_{\text{slice}}} \left\{ \sum_{\ell=1}^L C_{\ell,sl}(x,y)K_{\ell,j,z}(x,y) \right\} \rho_{sl}(x,y)
 \end{aligned}
 \tag{A5}$$

where $C_{j,z}(x,y)$ is the coil sensitivity profile of the j th coil at slice position z and $\rho_z(x,y)$ is the underlying image of slice z and $\rho_{\text{collapse}}(x,y)$ is the underlying image in the collapsed image. For the $N_{\text{slice}} = 2$ case, this becomes

$$\begin{aligned}
 C_{j,z}(x,y)\rho_z(x,y) &= \left\{ \sum_{\ell=1}^L C_{\ell,1}(x,y)K_{\ell,j,z}(x,y) \right\} \rho_1(x,y) \\
 &+ \left\{ \sum_{\ell=1}^L C_{\ell,2}(x,y)K_{\ell,j,z}(x,y) \right\} \rho_2(x,y)
 \end{aligned}
 \tag{A6}$$

Note that this governing equation, and hence the resulting slice-GRAPPA kernels, is dependent on the underlying images. This is in contrast to conventional GRAPPA and has several implications if this dependency is strong. For example, the same image contrast parameters must be used in the single-slice training data as in the slice-aliased data. This is particularly problematic for diffusion imaging where each diffusion direction could require a distinct kernel set. Fortunately, typical kernels fit to brain data satisfy a special case of Eq. A6, which preserves the anatomy independence of the GRAPPA operators. We show that under typical imaging conditions, the governing equation simplifies to the following two conditions where the dependence on the underlying image is no longer present:

$$C_{j,z}(x,y) = \sum_{\ell=1}^L C_{\ell,z}(x,y)K_{\ell,j,z}(x,y)
 \tag{A7}$$

$$0 = \sum_{\ell=1}^L C_{\ell,sl}(x,y)K_{\ell,j,z}(x,y), \quad \text{for all } sl \neq z
 \tag{A8}$$

For $N_{\text{slice}} = 2$ and $z = 1$ case, Eqs. A7 and A8 satisfy the Eq. A6 by requiring the first term in Eq. A6 to satisfy the equation and the second term to be zero. With these

conditions, the GRAPPA kernels are no longer dependent on the underlying images and are similar to conventional GRAPPA where the kernels are based only on the relationships between the coil sensitivity patterns.

A simple analysis can be performed to test the validity of Eqs. A7 and A8. We will illustrate this on a standard two simultaneous multislice acquisition example. In this test, the kernels used to generate the coil data for a given slice is applied to single-slice training data. First, it is applied to the single-slice data of the slice it was intended to generate. If Eq. A7 holds, it should regenerate this slice perfectly. Second, it is applied to the single-slice data of the slice it was not intended to generate. If Eq. A8 holds, this generated image should be 0. The test steps are as follows.

1. Train the GRAPPA kernels using a training dataset (i.e., a fully sampled dataset). Here, two sets of kernels are created ($K_{\ell,j,1}$ and $K_{\ell,j,2}$), one for each imaging slice.
2. Test Eq. A7: Apply $K_{\ell,j,1}$ kernels to data from slice 1 and $K_{\ell,j,2}$ kernels to data from slice 2. This will result in the following set of images:

$$I_{j,(1,1)}(x,y) = \sum_{\ell=1}^L C_{\ell,1}(x,y)\rho_1(x,y)K_{\ell,j,1}(x,y)$$

$$I_{j,(2,2)}(x,y) = \sum_{\ell=1}^L C_{\ell,2}(x,y)\rho_2(x,y)K_{\ell,j,2}(x,y)$$

where $I_{j,(s_{\text{kernel}},s_{\text{image}})}$ is the image from coil j th generated by applying the GRAPPA kernel set $K_{\ell,j,s_{\text{kernel}}}$ to the data from image slice s_{image} . If Eq. A7 is true then these images become

$$I_{j,(1,1)}(x,y) = C_{j,1}(x,y)\rho_1(x,y)$$

$$I_{j,(2,2)}(x,y) = C_{j,2}(x,y)\rho_2(x,y)$$

for all j coils. The left-hand side of Fig. A3b illustrates the result of this test, where the sum of square images of slices 1 and 2 are shown before and after the application of the GRAPPA kernel. The before and after images appear to be near identical, confirming that Eq. A7 is well satisfied.

3. Test Eq. A8: Apply $K_{\ell,j,2}$ kernels to data from slice 1 and $K_{\ell,j,1}$ kernels to data from slice 2. This will result in the following images:

$$I_{j,(1,2)}(x,y) = \sum_{\ell=1}^L C_{\ell,2}(x,y)\rho_2(x,y)K_{\ell,j,1}(x,y)$$

$$I_{j,(2,1)}(x,y) = \sum_{\ell=1}^L C_{\ell,1}(x,y)\rho_1(x,y)K_{\ell,j,2}(x,y)$$

If Eq. A8 is true then these images should all be zeros. The right-hand side of Fig. A3b illustrates this. Here, the images after the application of the GRAPPA kernels are scale up by $20\times$ to show very minor intensity deviation. Therefore, Eq. A8 is also well satisfied.

The intuition behind why Eqs. A7 and A8 can be expected to hold is obtained by revisiting the original

governing equation for $N_{\text{slice}} = 2$ (in Eq. A6). The governing equation for slice 1 is

$$C_{j,1}(x,y)\rho_1(x,y) = \left\{ \sum_{\ell=1}^L C_{\ell,1}(x,y)K_{\ell,j,1}(x,y) \right\} \rho_1(x,y) + \left\{ \sum_{\ell=1}^L C_{\ell,2}(x,y)K_{\ell,j,1}(x,y) \right\} \rho_2(x,y).$$

For the second term to be non-zero, the factor $\left\{ \sum_{\ell=1}^L C_{\ell,2}(x,y)K_{\ell,j,1}(x,y) \right\}$ needs to approximate $C_{j,1}(x,y)\rho_1(x,y)/\rho_2(x,y)$. In general, the ratio of two slices, $\rho_1(x,y)/\rho_2(x,y)$, is not smooth and contains high-frequency components which cannot be well approximated by the GRAPPA kernels and coil sensitivity profiles. It is simpler for the fitting process to make $\left\{ \sum_{\ell=1}^L C_{\ell,2}(x,y)K_{\ell,j,1}(x,y) \right\}$ fit a spatial constant (e.g., zero). Therefore, in the kernel fitting process, it is considerably easier to form GRAPPA kernels which make $\left\{ \sum_{\ell=1}^L C_{\ell,2}(x,y)K_{\ell,j,1}(x,y) \right\} = 0$ and thus satisfy the conditions of Eq. A8. Once Eq. A8 is satisfied, the governing equation reduces to $C_{j,1}(x,y) = \sum_{\ell=1}^L C_{\ell,1}(x,y)K_{\ell,j,1}(x,y)$, exactly that required by Eq. A7.

This same analysis holds for the cases of simultaneous multislice acquisition with interslice image shift. In such cases, the only modification to the governing equation is that the coil sensitivities and underlying images of the different slices are now shifted relative to one another.

REFERENCES

1. Lindquist MA, Zhang CH, Glover G, Shepp L. Rapid three-dimensional functional magnetic resonance imaging of the initial negative BOLD response. *J Magn Reson* 2008;191 (1):100–111.
2. Sodickson DK, Manning WJ. Simultaneous acquisition of spatial harmonics (SMASH): fast imaging with radiofrequency coil arrays. *Magn Reson Med* 1997;38 (4):591–603.
3. Pruessmann KP, Weiger M, Scheidegger MB, Boesiger P. SENSE: sensitivity encoding for fast MRI. *Magn Reson Med* 1999;42 (5):952–962.
4. Griswold MA, Jakob PM, Heidemann RM, Nittka M, Jellus V, Wang J, Kiefer B, Haase A. Generalized autocalibrating partially parallel acquisitions (GRAPPA). *Magn Reson Med* 2002;47 (6):1202–1210.
5. Mansfield P, Coxon R, Hykin J. Echo-volumar imaging (EVI) of the brain at 3.0 T: first normal volunteer and functional imaging results. *J Comput Assist Tomogr* 1995;19 (6):847–852.
6. van der Zwaag W, Francis S, Bowtell R. Improved echo volumar imaging (EVI) for functional MRI. *Magn Reson Med* 2006;56 (6):1320–1327.
7. Rabrait C, Ciuciu P, Ribes A, Poupon C, Le Roux P, Dehaene-Lambertz G, Le Bihan D, Lethimonnier F. High temporal resolution functional MRI using parallel echo volumar imaging. *J Magn Reson Imaging* 2008;27 (4):744–753.
8. Witzel T, Polimeni JR, Wiggins GC, Lin F-H, Biber S, Hamm M, Seethamraju R, Wald LL. Single-shot echo-volumar imaging using highly parallel detection. In: Proceedings of the 16th annual meeting of ISMRM, Toronto, Canada, 2008. p 2367.
9. Weaver JB. Simultaneous multislice acquisition of MR images. *Magn Reson Med* 1988;8 (3):275–284.
10. Paley MN, Lee KJ, Wild JM, Griffiths PD, Whitby EH. Simultaneous parallel inclined readout image technique. *Magn Reson Imaging* 2006;24 (5):557–562.
11. Wu EL, Chen J-H, Chiueh T-D. Wideband MRI: a new dimension of MR image acceleration. In: Proceedings of the 17th annual meeting of ISMRM, Hawaii, USA, 2009. p 2678.
12. Feinberg DA, Reese TG, Wedeen VJ. Simultaneous echo refocusing in EPI. *Magn Reson Med* 2002;48 (1):1–5.

13. Reese TG, Benner T, Wang R, Feinberg DA, Wedeen VJ. Halving imaging time of whole brain diffusion spectrum imaging and diffusion tractography using simultaneous image refocusing in EPI. *J Magn Reson Imaging* 2009;29 (3):517–522.
14. Larkman DJ, Hajnal JV, Herlihy AH, Coutts GA, Young IR, Ehnholm G. Use of multicoil arrays for separation of signal from multiple slices simultaneously excited. *J Magn Reson Imaging* 2001;13 (2):313–317.
15. Breuer FA, Blaimer M, Heidemann RM, Mueller MF, Griswold MA, Jakob PM. Controlled aliasing in parallel imaging results in higher acceleration (CAIPIRINHA) for multi-slice imaging. *Magn Reson Med* 2005;53 (3):684–691.
16. Nunes RG, Hajnal JV, Golay X, Larkman DJ. Simultaneous slice excitation and reconstruction for single shot EPI. In: Proceedings of the 14th annual meeting of ISMRM, Seattle, Washington, USA, 2006. p 293.
17. Moeller S, Yacoub E, Olman CA, Auerbach E, Strupp J, Harel N, Ugurbil K. Multiband multislice GE-EPI at 7 Tesla, with 16-fold acceleration using partial parallel imaging with application to high spatial and temporal whole-brain fMRI. *Magn Reson Med* 2010;63 (5):1144–1153.
18. Setsompop K, Gagoski BA, Polimeni J, Witzel TW, Wedeen VJ, Wald LL. Blipped CAIPIRHINA for simultaneous multi-slice EPI with reduced g -factor penalty. In: Proceedings of the 18th annual meeting of ISMRM, Stockholm, Sweden, 2010. p 551.
19. Feinberg DA, Moeller S, Smith SM, Auerbach E, Ramanna S, Glasser MF, Miller KL, Ugurbil K, Yacoub E. Multiplexed echo planar imaging for sub-second whole brain fMRI and fast diffusion imaging. *PLoS One* 2010;5 (12):1–11.
20. Keil B, Triantafyllou C, Hamm M, Wald LL. Design optimization of a 32-channel head coil at 7 T. In: Proceedings of the 18th annual meeting of ISMRM, Stockholm, Sweden, 2010. p 1493.
21. Feinberg DA, Jakob PD. Tissue perfusion in humans studied by Fourier velocity distribution, line scan, and echo-planar imaging. *Magn Reson Med* 1990;16 (2):280–293.
22. Reese TG, Heid O, Weisskoff RM, Wedeen VJ. Reduction of eddy-current-induced distortion in diffusion MRI using a twice-refocused spin echo. *Magn Reson Med* 2003;49 (1):177–182.
23. Blaimer M, Breuer FA, Seiberlich N, Mueller MF, Heidemann RM, Jellus V, Wiggins G, Wald LL, Griswold MA, Jakob PM. Accelerated volumetric MRI with a SENSE/GRAPPA combination. *J Magn Reson Imaging* 2006;24 (2):444–450.
24. Robson PM, Grant AK, Madhuranthakam AJ, Lattanzi R, Sodickson DK, McKenzie CA. Comprehensive quantification of signal-to-noise ratio and g -factor for image-based and k -space-based parallel imaging reconstructions. *Magn Reson Med* 2008;60 (4):895–907.
25. Smith SM, Jenkinson M, Woolrich MW, Beckmann CF, Behrens TE, Johansen-Berg H, Bannister PR, De Luca M, Drobnjak I, Flitney DE, Niazy RK, Saunders J, Vickers J, Zhang Y, De Stefano N, Brady JM, Matthews PM. Advances in functional and structural MR image analysis and implementation as FSL. *Neuroimage* 2004;23 (Suppl 1):S208–S219.
26. Behrens TE, Woolrich MW, Jenkinson M, Johansen-Berg H, Nunes RG, Clare S, Matthews PM, Brady JM, Smith SM. Characterization and propagation of uncertainty in diffusion-weighted MR imaging. *Magn Reson Med* 2003;50 (5):1077–1088.
27. Dale AM, Buckner RL. Selective averaging of rapidly presented individual trials using fMRI. *Hum Brain Mapp* 1997;5 (5):329–340.
28. Rooney WD, Johnson G, Li X, Cohen ER, Kim SG, Ugurbil K, Springer CS Jr. Magnetic field and tissue dependencies of human brain longitudinal $^1\text{H}_2\text{O}$ relaxation in vivo. *Magn Reson Med* 2007; 57 (2):308–318.
29. Bernstein MA, King KF. Handbook of MRI pulse sequences. Elsevier: Burlington, MA, 2004.
30. Johnson G, Wadghiri YZ, Turnbull DH. 2D multislice and 3D MRI sequences are often equally sensitive. *Magn Reson Med* 1999;41 (4): 824–828.
31. Breuer FA, Kannengiesser SA, Blaimer M, Seiberlich N, Jakob PM, Griswold MA. General formulation for quantitative G -factor calculation in GRAPPA reconstructions. *Magn Reson Med* 2009;62 (3):739–746.